

Signatures of multiple charge excitations in RIXS spectra of metals

I. S. Tupitsyn,¹ A. M. Tsvetik,² R. M. Konik,² and N. V. Prokof'ev¹

¹*Department of Physics, University of Massachusetts, Amherst, MA 01003, USA*

²*Condensed Matter Physics and Materials Science Division,
Brookhaven National Laboratory, Upton, NY 11973-5000, USA*

We study how multiple charge excitations appear in the resonant inelastic x-ray scattering (RIXS) spectra of metals. The single excitations in the problem are the plasmons and electron-hole pairs, and multi-excitation processes are usually neglected. However, at small momentum transfer the multi-excitation contributions may dominate the signal and one needs to understand how to interpret the data. In particular, we demonstrate how to "decode" the total multi-excitation intensity and extract the plasmon dispersion. While our calculations are based on the random phase approximation, which does not allow to obtain quantitatively precise results in the entire region of parameters, we expect them to capture semi-qualitatively all features expected for charged Fermi-liquid states, including universal and singular properties of the RIXS spectra.

I. INTRODUCTION

Resonant inelastic X-ray scattering (RIXS) is a very promising technique for studying collective excitations in condensed matter systems^{1–6}. However, extracting the necessary information from the RIXS data is a highly non-trivial task. The deep core-hole, created by an incident photon, disturbs the system which leads to a variety of multiparticle processes contributing to the measured RIXS signal. To extract the relevant information about excitations of interest, one needs to properly understand all the processes involved and be able to distinguish single- and multi-excitation processes.

The main goal of the RIXS measurements is to distill properties of single excitations (plasmons, phonons, magnons, *etc.*) and the majority of theoretical efforts concentrate on computing the corresponding single-excitation contributions to the RIXS intensity, neglecting the multi-excitation processes. However, these processes (typically characterized by rather broad frequency signals) also contain information about single excitations in some convoluted form and understanding their properties can be especially important when they dominate in the RIXS intensity. This turns out to be the case at small momentum transfer in Coulomb systems, see, for instance, Ref. 7). Moreover, studies of multiple excitations may prove to be a convenient practical way of extracting the underlying physics from the broad frequency signal provided their universal features and the corresponding singularities are well understood.

Even for single-excitation contributions to the RIXS signal, an accurate theoretical prediction requires knowledge of the dynamic dielectric response function, $\epsilon(\mathbf{q}, \omega)$, which is a difficult computational materials science problem; the problem becomes even more challenging when dealing with multi-excitation processes. On the other hand, significant qualitative and even semi-quantitative gains in description can be obtained by approximating the dielectric response with the analytic form based on the Lindhard function (equivalent to the random phase approximation (RPA)) which captures all the properties

characteristic of the charged Fermi-liquid state.

To illustrate the point, we present on Fig. 1 our results for the RIXS spectra due to all two-excitation processes (two plasmons, two electron-hole ($e-h$) pairs, and the hybrid process involving one plasmon and one $e-h$ pair). In Section V we will explain how one can extract the single-plasmon dispersion from the characteristic features of these curves. In Fig. 2 we compare the results of such analysis with the plasmon dispersion relations (at $r_s = 1$ and $r_s = 5$), based on the solution of equation $\epsilon(q, \omega_{pl}(q)) = 0$. Note that the spectra for weak and strong coupling cases look remarkably similar despite significant changes in the absolute values of all quantities.

There are several approaches for calculating the RIXS spectra^{8–11}, and in this work we follow the diagrammatic framework developed in Ref. 7 (for earlier diagrammatic works on RIXS see, for instance, Refs. 12–14; for Raman scattering see Ref. 15). Below we focus on the non-linear indirect RIXS spectra with arbitrary momentum transfer and the Coulomb parameter r_s up to $r_s = 5$ (with understanding that the RPA treatment is quantitatively accurate only for $r_s \lesssim 1$). All calculations are performed for $T = 0$ in the limit of short hole's life time (SHLT)⁷. Here and below we use units such that the Planck's constant, \hbar , the Fermi momentum, k_F , and the Fermi energy, ϵ_F , are set to unity.

Previous work⁷ discussed two-excitation spectra by employing a simplified description of the dielectric response function valid in the $q/k_F \ll 1$ limit. The two most important qualitative features not captured by this treatment were the singular behavior at momenta and frequencies corresponding to the end point of the plasmon dispersion relation, and the non-analyticity at $q = 2k_F$. Furthermore for the process involving two $e-h$ pairs even at small momentum and energy transfer one cannot ignore pairs with large momenta $\sim k_F$. To eliminate these deficiencies and achieve a comprehensive semi-quantitative description in a broad parameter range, including large energy and momentum transfer, one has to work with the entire Lindhard function.

In what follows we study the universal and singular properties of the two-excitation RIXS processes in a

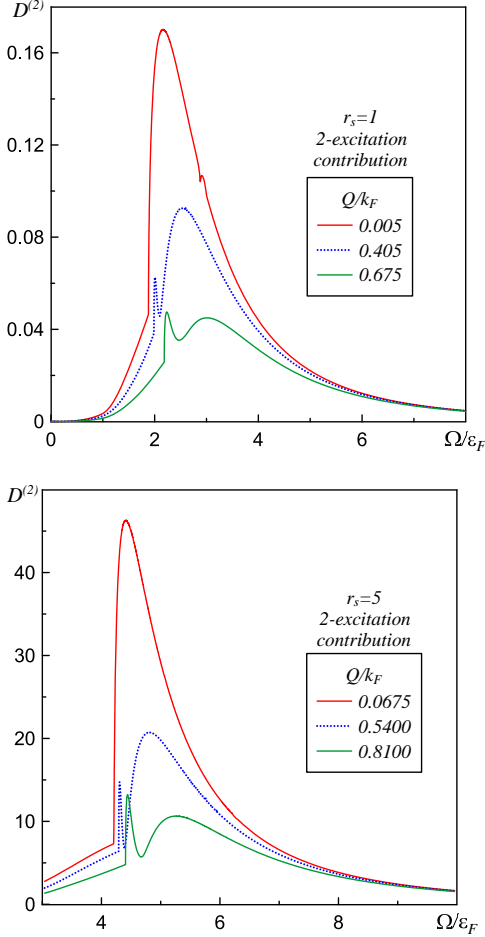


FIG. 1. (color online) Total two-excitation RIXS intensity as a function of energy transfer Ω . It includes two-plasmon, two- $(e-h)$, and the hybrid (see text) processes shown for several momentum transfers Q . Upper panel: $r_s = 1$. Lower panel: $r_s = 5$.

Coulomb plasma, where long-range interactions and dynamic screening effects are very important. We do not make any further approximations on the charge response function after assuming the RPA form for the polarization. We explain how the single-plasmon dispersion can be extracted from the total two-excitation intensity by relating various spectral features to important threshold processes, and establish the framework for interpreting complex spectra in terms of partial contributions. We conclude with demonstration how the total spectra, including first- and second-order processes, may appear in the experiment.

II. FORMALISM

Within the diagrammatic formalism of Ref. 7 the leading order diagrams for the RIXS cross section χ_R in the SSH limit are shown in Fig. 3. The first order (in the dynamically screened interaction U , see Fig. 3(b)) diagram shown in Fig. 3(a) describes the single-excitation contri-

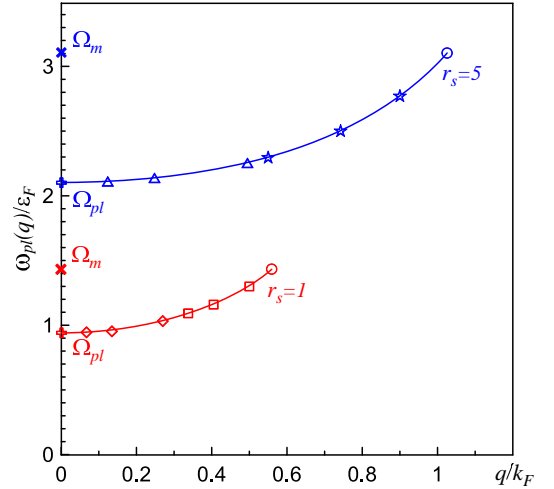


FIG. 2. (color online) A comparison of the plasmon dispersions $\omega_{pl}(q)$ for $r_s = 1$ (red solid line) and $r_s = 5$ (blue solid line) derived from the zeros of the dielectric function with the ones deduced from the two-excitation RIXS spectra shown in Fig. 1. The different symbols correspond to positions of different spectral features. $\Omega_{pl} = \omega_{pl}(0)$ is the plasma frequency and $\Omega_m = \omega_{pl}(Q_m)$ is the maximal plasma frequency. For details see Section V.

bution from plasmons and $e-h$ pairs. The second order diagrams, Figs. 3 (c) and (d), are responsible for contributions from the two-excitation processes involving either two plasmons, or two $e-h$ pairs, or one plasmon and one $e-h$ pair (we call the latter a hybrid process). Contributions from higher order multi-excitation processes are small in the hole's life time Γ^{-1} .

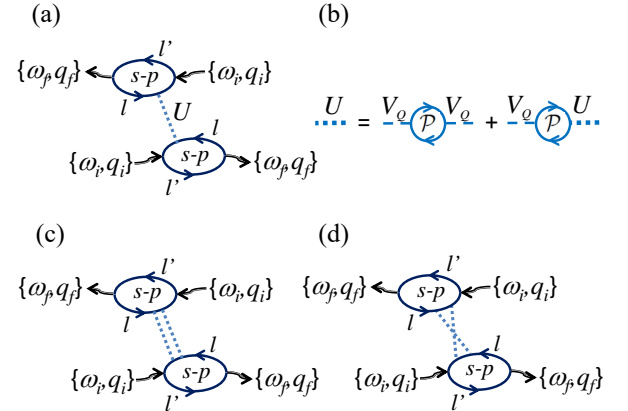


FIG. 3. (color online) The leading order diagrams for the RIXS cross section in the SHLT limit (e.g., for the K -edge case) with l and l' indexes standing for either s -hole, or p -electron, and $\{\omega_i, \mathbf{q}_i\}$ and $\{\omega_f, \mathbf{q}_f\}$ specifying the incoming and outgoing photon energies and momenta. The dynamically screened Coulomb potential U , shown by the blue dotted line, can connect any upper $s-p$ bubble line (s or p) with any lower $s-p$ bubble line; here, for brevity, we present only one particular way of connecting the bubbles.

The first-order contribution to the RIXS intensity for momentum, Q , and energy/frequency, Ω , transfer is given by

$$\chi_R^{(1)} = \frac{\Upsilon_1^2}{\Gamma^2} D^{(1)}(\Omega, Q) \quad (1)$$

with

$$D^{(1)} = f_1(\mathbf{Q}) \mathcal{I}mU(\Omega, Q), \quad (2)$$

where the dynamically screened Coulomb potential U is given by (see Fig. 3(b))

$$U(\Omega, Q) = \frac{V_Q}{1 - V_Q \mathcal{P}(\Omega, Q)} - V_Q; \quad V_Q = \frac{4\pi e^2}{Q^2} \quad (3)$$

and the form-factor, $f_1(\mathbf{Q})$ vanishes in the small momentum transfer limit⁷. For crystals with inversion symmetry it can be modeled by

$$f_1(\mathbf{Q}) = \left[\frac{Q^2}{Q^2 + Q_d^2} \right]^2. \quad (4)$$

with some characteristic momentum cutoff $Q_d \sim k_F$. In the SHLT limit the $(s-p)$ bubbles contribute a frequency independent factor and one can replace Υ_1 in Eq. 1 with a constant of the order of unity. In what follows, we will use $1/k_F$ and ε_F as units of length and energy and not mention them explicitly in dimensionless ratios Q/k_F and Ω/ε_F .

In contrast to Ref. 7, in the present paper the polarization function is described by the full Lindhard function^{16,17} in order to correctly capture all Fermi-surface effects and the interplay between the plasmon mode and the $e-h$ continuum

$$\begin{aligned} \mathcal{R}e\mathcal{P} = & \frac{3n}{4\varepsilon_F} \left[-1 + \frac{4Q^2 - Q_+^4}{8Q^3} \log \left| \frac{2Q + Q_+^2}{2Q - Q_-^2} \right| \right. \\ & \left. - \frac{4Q^2 - Q_+^4}{8Q^3} \log \left| \frac{2Q + Q_+^2}{2Q - Q_+^2} \right| \right], \end{aligned} \quad (5)$$

$$\mathcal{I}m\mathcal{P} = \frac{3\pi n}{8\varepsilon_F Q} \begin{cases} -\Omega & \text{if A;} \\ -[1 - (\Omega/Q - Q)^2/4] & \text{if B;} \\ -[1 - (\Omega/Q - Q)^2/4] & \text{if C;} \end{cases} \quad (6)$$

$$A : \quad Q < 2, \quad 0 \leq \Omega < -Q^2 + 2Q;$$

$$B : \quad Q < 2, \quad -Q^2 + 2Q \leq \Omega \leq Q^2 + 2Q;$$

$$C : \quad Q \geq 2, \quad Q^2 - 2Q \leq \Omega \leq Q^2 + 2Q,$$

where $Q_\pm^2 = \Omega \pm Q^2$ and $n = k_F^3/3\pi^2$. The definition of the Coulomb r_s parameter is standard: $e^2 = (r_s k_F/m)(4/9\pi)^{1/3}$.

For momenta $Q < Q_m$, the $\mathcal{I}mU \equiv \tilde{D}$ function can be naturally divided into two contributions $\tilde{D} = \tilde{D}_{e-h} + \tilde{D}_{pl}$: the first one is associated with the electron-hole continuum, and the other one with the gapped plasmon resonance that exists as a separate sharp mode only up to a finite momentum Q_m when it merges into the $e-h$

continuum. In terms of the real and imaginary parts of the polarization function, we have

$$\tilde{D}_{e-h} = \frac{\mathcal{I}m\mathcal{P}}{[(V_Q^{-1} - \mathcal{R}e\mathcal{P})^2 + (\mathcal{I}m\mathcal{P})^2]}, \quad (7)$$

$$\tilde{D}_{pl} = \pi \text{Res}[\omega_{pl}(Q)] \delta(\Omega - \omega_{pl}(Q)), \quad \mathcal{I}m\mathcal{P} = 0. \quad (8)$$

The plasmon peak frequency and residue are derived from properties of the dielectric function $\epsilon = 1 - V_Q \mathcal{P}$:

$$\epsilon(Q, \omega_{pl}(Q)) = 0; \quad \text{Res}[\omega] = \frac{1}{|\partial\epsilon/\partial\Omega|_\omega}, \quad (9)$$

see Fig. 4.

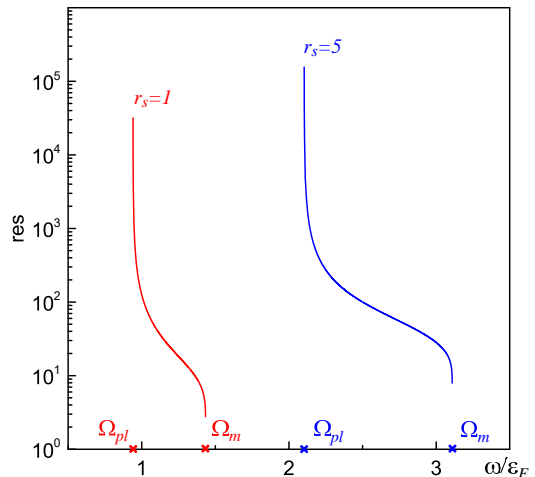


FIG. 4. (color online) Plasmon residue $\text{Res}(\omega)$ as a function of frequency for $r_s = 1$ and 5. At $\omega \rightarrow \Omega_{pl}$, $\text{Res}(\omega)$ behaves as $\propto 1/(\omega - \Omega_{pl})$; at $\omega \rightarrow \Omega_m$, $\text{Res}(\omega) - \text{Res}(\Omega_m) \propto \sqrt{\Omega_m - \omega}$.

The second-order contribution to the RIXS intensity reads

$$\chi_R^{(2)} = \frac{\Upsilon_2^2}{\Gamma^4} D^{(2)}(\Omega, Q), \quad (10)$$

with frequency independent constant $\Upsilon_2 \sim 1$ and

$$D^{(2)} = \int \frac{d\mathbf{q}d\omega}{(2\pi)^4} f_2(\mathbf{q}, \mathbf{Q} - \mathbf{q}) \tilde{D}(\omega, \mathbf{q}) \tilde{D}(\Omega - \omega, \mathbf{Q} - \mathbf{q}), \quad (11)$$

where the model form-factor

$$f_2(\mathbf{q}_1, \mathbf{q}_2) = \frac{(\mathbf{q}_1 \cdot \mathbf{q}_2)^2}{(q_1^2 + Q_d^2)(q_2^2 + Q_d^2)}. \quad (12)$$

is designed to respect the small momentum transfer dependence coming from the $(s-p)$ bubbles for the sum of two second-order diagrams (see Figs. 3 (b) and (c)). Below we set $\Upsilon_{1,2} = 1$ and present all results without the Γ factors.

III. SINGLE-EXCITATION PROCESSES

Here we briefly review the known properties of \tilde{D} . There is no point in showing the plasmon contribution

because it is completely characterized by the dispersion relation and the pole residue, see Eq. (9) and Fig. (2) and (4). The $e-h$ pair contribution results in a broad spectral curve with intensity diverging on the approach to the end point of the plasmon spectrum, see Fig. 5. The upper threshold of the $e-h$ spectrum is located at

$$\Omega_{e-h}(Q) = v_F Q + \frac{Q^2}{2m}. \quad (13)$$

The end point of the plasmon dispersion is then defined by the condition $\Omega_{e-h}(Q_m) = \Omega_m$ leading to the following relation for Ω_m :

$$\Omega_m = \omega_{pl}(Q_m) = v_F Q_m + \frac{Q_m^2}{2m}. \quad (14)$$

For $r_s = 1$ and $r_s = 5$ the largest plasmon momentum equals to $Q_m = 0.560 k_F$ and $Q_m = 1.027 k_F$, respectively.

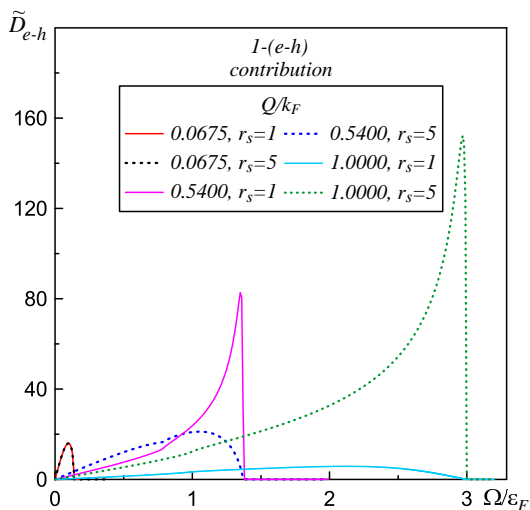


FIG. 5. (color online) Single pair contribution to intensity, \tilde{D}_{e-h} , as a function of Ω for different values of momentum transfer Q at $r_s = 1$ (solid lines) and 5 (dotted lines). The $f_1(Q)$ factor is removed.

At small momenta Q the shapes of the \tilde{D}_{e-h} curves for different values of r_s are nearly indistinguishable. With increasing Q the peak amplitude increases until $Q = Q_m$, where the $e-h$ continuum “absorbs” the plasmon mode. At $Q > Q_m$ the peak maximum decreases while the plasmon contribution no longer exists. For $r_s = 1$ the $Q = k_F$ case corresponds to $Q > Q_m$ when the intensity is already rather small, featureless, and broad; for $r_s = 5$ this momentum transfer is slightly below the plasmon end-point, $Q < Q_m$, and the intensity keeps increasing in a singular fashion.

At the RPA level, there is a certain degree of universality in the scaled shapes of the curves for small and large values of r_s . It is clear from Fig. 5 that large values of r_s do not introduce new spectral features; in general, only the positions of peaks and their intensities are

changed. To verify this quantitatively, in Fig. 6 the $e-h$ contributions for $r_s = 1$ and $r_s = 5$ are presented for momentum transfers corresponding having the same Q/Q_m ratio close to unity. The curves are scaled to have the same peak amplitude and are plotted as functions of the Ω/Ω_m . It is clear that the characteristic features of the $e-h$ contribution, shown in Fig. 5 and described above, barely change as a function of r_s .

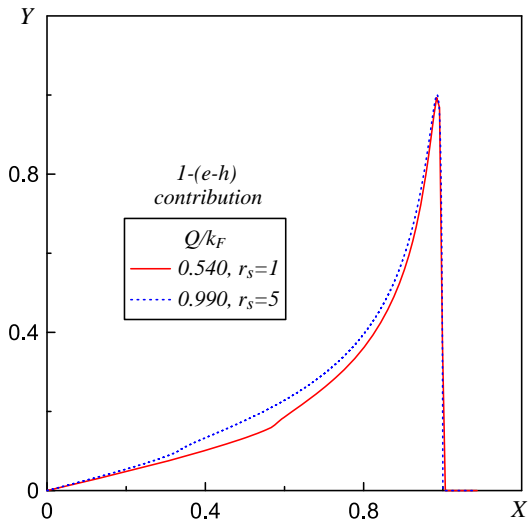


FIG. 6. (color online) Scaled single-pair contributions to intensity, $Y = \tilde{D}_{e-h}/\{\tilde{D}_{e-h}\}_{max}$, as functions of $X = \Omega/\Omega_{e-h}(Q)$ for $r_s = 1$ and $r_s = 5$ (with the same $Q/Q_m \approx 0.964$ ratio for both curves). The $f_1(Q)$ factor is removed.

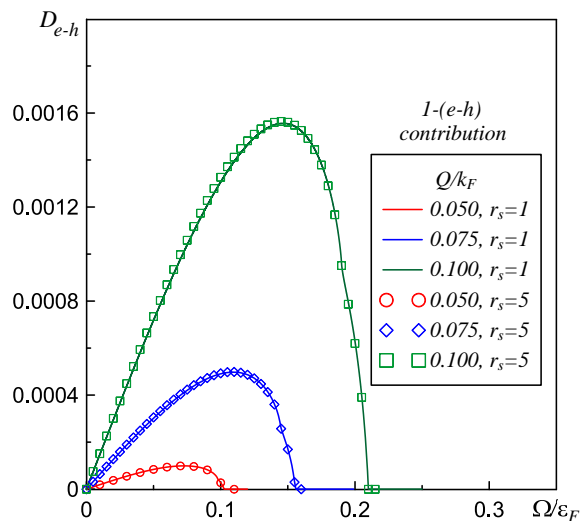


FIG. 7. (color online) Single-pair contributions to intensity as functions of Ω at $r_s = 1$ and 5 when $Q/Q_m \ll 1$ for both curves. The $f_1(Q)$ factor is not removed, in contrast to Figs. 5 and 6 - this allows to see the actual values of the $e-h$ intensity (without the Γ factor).

At small momentum (and energy) transfer the $e-h$ intensity curves become independent of r_s , see Fig. 7. At

$\Omega \ll v_F Q$ they are linear in Ω and the amplitude is proportional to Q^3 . The intensity of the plasmon peak under the same conditions is proportional to $r_s^{3/2} Q^2$. These scaling laws imply that at small Q the single-excitation RIXS spectrum can be weak and potentially subdominant to higher-order processes considered next.

IV. MULTI-EXCITATION PROCESSES

In the SHLT limit the higher-order processes are suppressed because they involve additional powers of the small parameter $(\Omega_{pl}/\Gamma)^2 \ll 1^7$. However, at small momentum transfer the second-order processes can dominate the spectrum even in the region where the first-order intensity is non-zero because the form factor f_2 has a different dependence on Q , see Eq. (12). As it has already been noted in the Introduction, despite having a more complex and convoluted shape, the two-excitation spectra can be used to extract information about single excitations provided the origin of their characteristic features is well understood.

By substituting equations (7) and (8) into equation (11) we obtain partial (two-plasmon, two-($e-h$), and hybrid) contributions to the total intensity. In what follows we first address each process separately and then conclude with the discussion of the total two-excitation intensity.

A. Two-plasmon process

In contrast to the sharp single-plasmon peak located at $\omega_{pl}(Q)$, the two-plasmon spectrum is broad - it starts at $2\omega_{pl}(Q/2)$ and terminates at $2\Omega_m$. Even for $Q = 0$ the two-plasmon spectrum is well outside of the single-plasmon dispersion range, see Fig. 2; i.e., the single- and two-plasmon spectra do not overlap. However, single-pair and two-plasmon peaks can overlap at large momentum transfer.

Apart from the thresholds, there are two singular points in spectrum, corresponding to two sets of momenta \mathbf{q}_1 and \mathbf{q}_2 of two plasmons: $(q_i = 0, q_j = Q)$ and $(q_i = Q_m, q_j = Q_m - Q)$, where $i \neq j = 1, 2$. At the first singular point the spectrum vanishes because $f_2(\mathbf{q}_1, \mathbf{q}_2) = 0$, see Eqs. (11)-(12). This minimum is located at

$$\Omega_{lm} = \Omega_{pl} + \omega_{pl}(Q). \quad (15)$$

and is clearly seen on the two-plasmon curves in their lower-frequency part, see both panels of Fig. 8, and is preceded by a maximum for obvious reasons. When $Q \rightarrow 0$, the minimum is approaching the low-energy threshold and the spectral weight displays a sharp low-amplitude oscillation. At $Q > Q_m/2$ the minimum broadens and at $Q > Q_m$ completely reshapes the spectrum.

At the second singular point there is no special reason for the two-plasmon spectrum to vanish; instead, it is seen as a kink located at

$$\Omega_{rk} = \Omega_m + \omega_{pl}(Q_m - Q). \quad (16)$$

It is more pronounced on small-to-moderate- Q curves (when the low-frequency maximum is smaller in intensity than the central one) in their high-frequency part, see both panels of Fig. 8. At $Q \rightarrow 0$ the kink is approaching the high-frequency threshold at $2\Omega_m$, while for $Q > Q_m$ it disappears together with the central maximum.

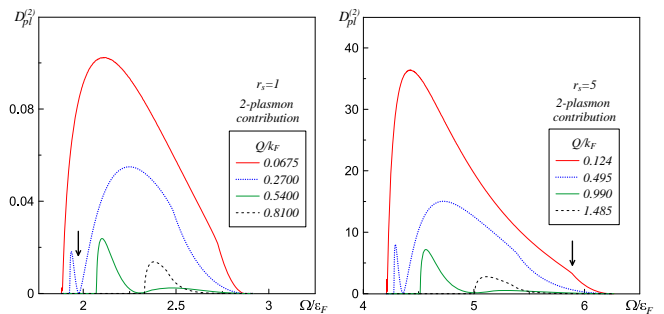


FIG. 8. (color online) Two-plasmon contributions to intensity for several values of Q . Left panel: $r_s = 1$, the arrow points at the low-frequency minimum. Right panel: $r_s = 5$, the arrow points at the high-frequency kink.

Disregarding the overall amplitude of the signal, the two-plasmon curves for $r_s = 1$ and 5 look very similar and in RPA the non-perturbative values of r_s do not introduce new features to the two-plasmon spectra. To quantify this statement further, in Fig. 9 we compare spectra for $r_s = 1$ and $r_s = 5$ using properly scaled variables: the momentum transfer was chosen to have the same ratio for $Q/Q_m(r_s)$, the intensity was normalized to unity at the maximum, and the frequency was scaled to be in the $[0, 1]$ interval.

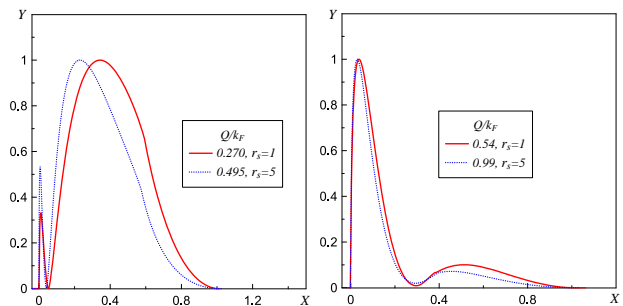


FIG. 9. (color online) Scaled two-plasmon intensities $Y = D_{pl}^{(2)}/\{D_{pl}^{(2)}\}_{max}$ as functions of $X = [\Omega - 2\Omega(Q/2)]/2[\Omega_m - \Omega(Q/2)] \in [0, 1]$ for $r_s = 1$ and $r_s = 5$. The momentum transfer for two cases was adjusted to have the same ratio $Q/Q_m(r_s)$.

It is also worth mentioning that for the two-plasmon process, the intensity at the central maximum saturates

to a constant when $Q \rightarrow 0$ while the spectrum remains broad, in contrast to the $\propto Q^2$ spectral weight scaling associated with the single-plasmon process.

B. Hybrid processes

The thresholds for the hybrid spectrum are at Ω_{pl} and $\Omega_m + \Omega_{e-h}(Q_m + Q)$, as dictated by the energy-momentum conservation laws and limited momentum support for the plasmon dispersion. At $Q \rightarrow 0$ the upper threshold is located at $2\Omega_m$ (see Eq. 14). In Fig. 10 we show the hybrid spectra for $r_s = 1$ and $r_s = 5$. Since the lower threshold is at the plasma frequency Ω_{pl} , the hybrid spectrum overlaps either with the single-plasmon, or with the single-pair spectrum. At $Q \rightarrow 0$ the intensity of the broad central maximum saturates to a constant, in contrast to the $\propto Q^3$ scaling of the shrinking single-pair spectrum and $\propto Q^2$ scaling of the single-plasmon weight. However, since the hybrid intensity vanishes at $\Omega \rightarrow \Omega_{pl}$, it does not obscure the sharp single-plasmon peak in the $Q \rightarrow 0$ limit (contrary to the two-pair process discussed next).

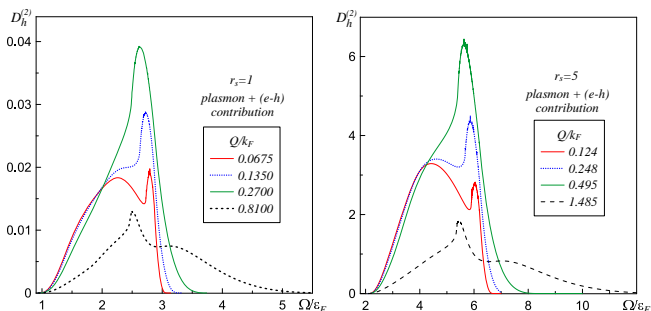


FIG. 10. (color online) Hybrid contribution to intensity as a function of Ω for several values of Q at $r_s = 1$ (left panel) and $r_s = 5$ (right panel).

At $Q > 0$ the high-frequency peak emerges from the threshold, grows in amplitude, see Fig. 11, and ultimately reshapes the entire curve, see Fig. 10. The origin of this peak at small Q can be traced to the fact that near the upper threshold the pair and plasmon excitations both have momenta close to Q_m in modulus but pointing in the opposite directions. The peak develops from the interplay between the singularities in the plasmon peak residue and pair intensity when $\Omega \rightarrow \Omega_m$, see Figs. 4 and 6, and the available phase-space volume. It is not an accident that the emerging hybrid peak location correlates with the location of the kink on the two-plasmon curve because for $Q \rightarrow Q_m$ the single-pair spectrum intensity diverges on approach to Ω_m mimicking a plasmon resonance.

Again, the curves for different values of r_s in Fig. 10 appear similar, and this observation can be quantified by plotting the data using scaled variables as it was done for the two-plasmon process. The result is presented in

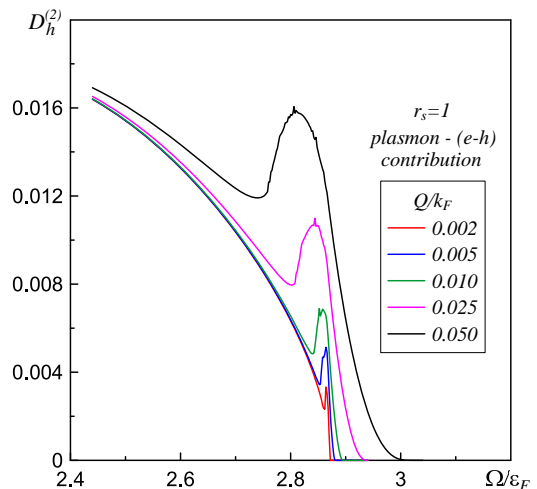


FIG. 11. (color online) Hybrid contribution to intensity: $D_h^{(2)}$ as a function of Ω at small values of Q and $r_s = 1$.

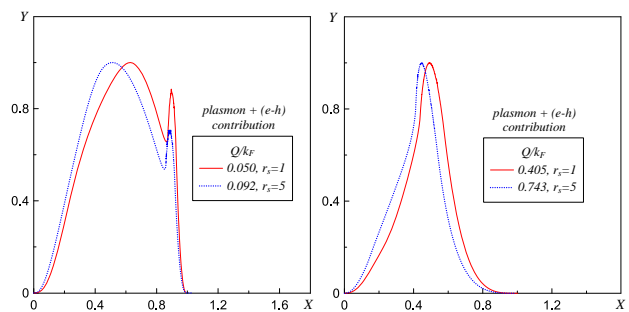


FIG. 12. (color online) Scaled hybrid contributions to intensity for $r_s = 1$ and $r_s = 5$. The data are plotted for $Y = D_h^{(2)} / \{D_h^{(2)}\}_{max}$ as functions of $X = [\Omega - \Omega_{pl}] / [\Omega_m + \Omega_{e-h}(Q_m + Q) - \Omega_{pl}] \in [0, 1]$. The momentum transfer for two cases was adjusted to have the same ratio Q/Q_m .

Fig. 12. The intensity of the hybrid process does not vanish at $Q \rightarrow 0$; however, its features are difficult to observe because of interplay with the two-pair process discussed below. Nevertheless, the upper threshold of the hybrid contribution is visible on total curves at small values of momentum transfer which gives access to information about the single $e - h$ process.

C. Two-pair processes

The last process contributing to the second-order spectra is the two-pair one. The result is expected to be a smooth peak. The typical shapes are presented in Fig. 13—they start at $\Omega = 0$ and at large frequency demonstrate an asymptotic $\sim \Omega^{-7/2}$ decay. At small frequencies, the signal is proportional to Ω^2 , as expected from the single-pair intensity $\propto \Omega$ at $\Omega \rightarrow 0$.

The maximum at small momenta is located close to $2\Omega_m$, where the two-plasmon and hybrid processes have

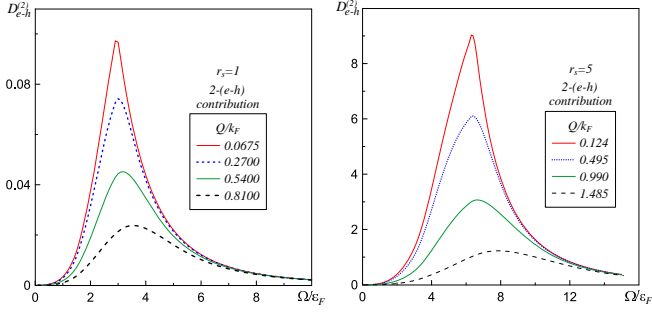


FIG. 13. (color online) Two-pair contribution intensity as a function of Ω for several values of Q at $r_s = 1$ (left panel) and 5 (right panel).

the kink and the high-frequency peak, respectively. The intensity maximum saturates to a constant in the $Q \rightarrow 0$ limit, implying that in this limit the entire RIXS spectrum is dominated by the second-order processes. By comparing the two-pair contribution to other second-order processes, we see that the former dominates the total two-excitation spectrum in the low- and high-frequency parts. By comparing curves in the left and right panels of Fig. 13 we observe similar universality as for other second-order processes.

D. Total two-excitation intensities

By combining all second-order processes we obtain the total two-excitation intensity, see Fig. 14. It is expected that some of the features clearly seen on individual curves may be masked when different contributions overlap. At low ($\Omega \lesssim \Omega_{pl}$) and high ($\Omega \gtrsim 2\Omega_m$) frequencies the total signal is dominated by the two-pair process. At intermediate frequencies the leading contribution often comes from the two-plasmon process which is responsible for sharp features at $Q \lesssim Q_m$, see Figs. 15 and 1.

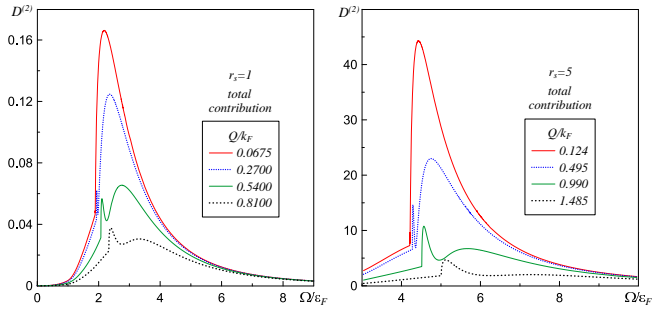


FIG. 14. (color online) Total second-order intensity as a function of Ω for several values of Q at $r_s = 1$ (left panel) and 5 (right panel).

In Fig. 15 we present the central part of the spectrum and compare all partial and total signals side-by-side

order to understand how spectral features in the final result should be “decoded”. The low-frequency kink and minimum are due to the two-plasmon process and these sharp features remain clearly visible, while the lower threshold for the hybrid process is masked by the two-pair contribution. The high frequency kink in the two-plasmon spectrum (best seen in two left panels in Fig. 15) is compensated by the non-monotonous dependence of the hybrid process and is not visible on total curves.

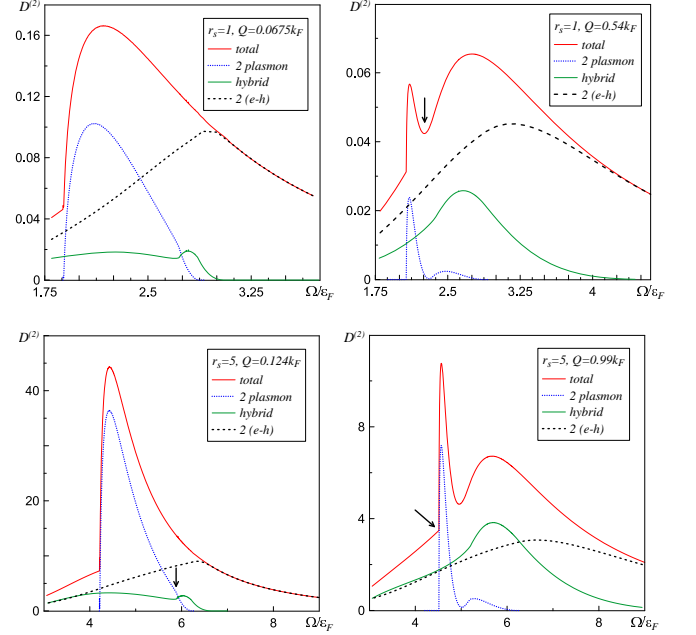


FIG. 15. (color online) Total and all partial (two-plasmon, two-pairs, and hybrid) contributions to intensity as a function of Ω . Upper left panel: $r_s = 1$ and $Q = 0.0675k_F$; the arrow points at the high-frequency kink on the two-plasmon curve. Upper right panel: $r_s = 1$ and $Q = 0.54k_F$; the arrow points at the low-frequency minimum. Lower left panel: $r_s = 5$ and $Q = 0.124k_F$; the arrow points at the high-frequency kink on the two-plasmon curve. Lower right panel: $r_s = 5$ and $Q = 0.99k_F$; the arrow points at the low-frequency kink.

The interplay between the sharp non-monotonous hybrid signal at high frequencies (see Fig. 11) and the two-pair intensity maximum results in a wiggly-like spectral anomaly seen in Fig. 16 at around $2\Omega_m$. This anomaly is pronounced only at small momenta and disappears at larger values of Q , see Fig. 17. The position of the developing at $Q \rightarrow 0$ minimum corresponds to the upper threshold of the hybrid process.

As it has already been mentioned, the two-plasmon high-frequency kink is not seen on the total curve, due to the interplay between the two-plasmon and hybrid processes. This is because these processes are characterized by the kink and anti-kink features that compensate each other (since the plasmon peak at $Q = Q_m$ is getting absorbed by the $e - h$ continuum without change in the total spectral weight).

Obviously, the universality of all features established

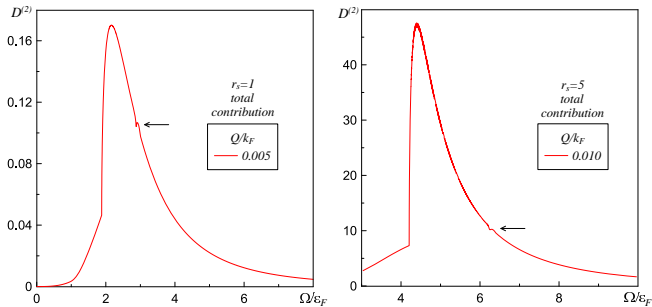


FIG. 16. (color online) Total second-order intensity as a function of Ω for small values of Q at $r_s = 1$ (left panel) and 5 (right panel). The arrows point at the wiggly-like spectral anomaly appearing at small momentum transfer as the result of interplay between the high frequency hybrid signal near its threshold and the two-pair intensity maximum.

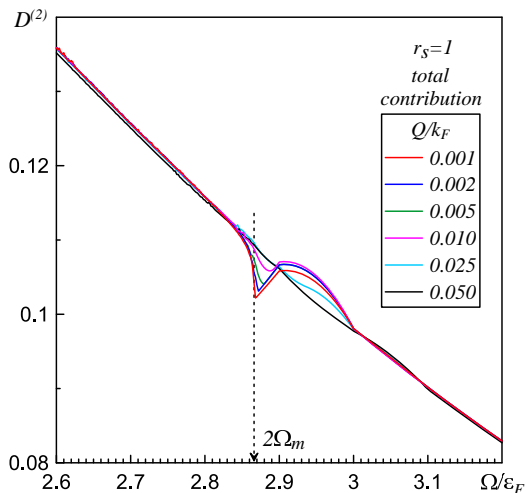


FIG. 17. (color online) Total second-order intensity in the vicinity of the $2\Omega_m$ frequency for progressively smaller values of Q at $r_s = 1$ demonstrating the development of the wiggly-like spectral anomaly.

for partial contributions carries through to the total intensity. However, as it has already been mentioned, the overlap of partial contributions at different values of momenta transfer may mask some features.

V. RESOLVING THE PLASMON DISPERSION FROM THE TOTAL TWO-EXCITATION INTENSITY

The distinct features on the total two-excitation intensity curves, shown in Figs. 15, 16, and 17, provide enough information for extracting the entire single-plasmon dispersion. The position of the low-frequency minimum on two-plasmon curves is given by Eq. (15). This expression can be used right away since the dispersion starts at the plasma frequency $\Omega_{pl} = \sqrt{4\pi ne^2/m}$. This gives $\omega_{pl}(Q) = \Omega_{lm} - \Omega_{pl}$, where Ω_{lm} is the minimum position. Note, however, that at $Q > Q_m/2$ the exact po-

sition of the low-frequency minimum on the total curve is no longer determined solely by the 2-plasmon contribution since it becomes relatively broad and derivatives from the other two processes shift it. Thus, it is best to restrict the plasmon dispersion analysis using this spectral feature to data for $Q \leq Q_m/2$. This is not a problem since the second half of the $[0, Q_m]$ interval can be covered by measuring $2\omega_{pl}(Q/2)$ from the threshold of the two-plasmon spectrum (low-frequency kink shown by the arrow in the lower right panel of Fig. 15). This feature is very sharp and provides accurate data all the way to $Q \lesssim 2Q_m$.

One also needs to know the end-point of plasmon dispersion, $\Omega_m = \omega_{pl}(Q_m)$ (from Ω_m one can easily find Q_m via (13) and (14)). Ω_m can be found by measuring the intensity around the spectral anomaly at $Q \rightarrow 0$, see Figs. 16 and 17. At $Q = 0$ the anomaly is located precisely at $2\Omega_m$. At small but finite Q , the anomaly's minimum position is determined by the upper threshold of the hybrid process, $\Omega_m + \Omega_{e-h}(Q_m + Q)$. This then gives access to information about single $e-h$ processes.

An alternative way to measure Q_m and Ω_m is to look at the $Q \lesssim Q_m$ single-pair process which is not supposed to be masked by the multi-excitation processes. By determining at which momentum Q the single-pair intensity at the maximum starts to decrease, one can locate Q_m and, correspondingly, Ω_m (see Section III).

To get the dispersion curves shown in Fig. 2, we have only used positions of the low-frequency minimum and the low-frequency kink. For $r_s = 1$ we have considered points $Q/k_F = 0.0675, 0.135, 0.27, 0.675, 0.81, 1.0$ while for $r_s = 5$ we have used $Q/k_F = 0.124, 0.248, 0.495, 1.10, 1.485, 1.80$. The two different sets of symbols on the dispersion curves correspond to applying Eqn. (15) (the equation governing the low-frequency minimum and used at lower frequencies) and $2\omega_{pl}(Q/2)$ (the position of the low-frequency kink and used at higher frequencies). Fig. 17 has been used to establish the value of Ω_m , and thus Q_m , see Eq.(14). For $r_s = 1$ and 5 we have reproduced $Q_m/k_F = 0.56$ and $Q_m/k_F = 1.027$, respectively ($\Omega_m/\varepsilon_F = 1.433$ and $\Omega_m/\varepsilon_F = 3.109$); in Fig. 2 these end points are marked by red and blue circles (red and blue crosses mark the start points, i.e. $\Omega_{pl}(r_s)$).

It is also worth mentioning that, depending on experimental conditions, narrow plasmon peaks may be hard to locate and the entire single-excitation intensity quickly vanishes at small momenta (see, for instance, Fig. 18 in Section VI).

VI. FIRST- VS SECOND-ORDER SPECTRA

To see how first- and second-order processes will appear in the experiment, we present Figs. 18 and 19. In Fig. 18 we plot the total spectra at small values of Q in the SHLT limit controlled by the small parameter $(\Omega_{pl}/\Gamma)^2$; since we do not know the exact value of that parameter, for the purpose of the presentation we

take it to be 0.1. To present data for the single-plasmon resonance, we assumed two experimental frequency resolutions, $\sigma = 0.01\varepsilon_F$ and $0.1\varepsilon_F$, by smearing the δ -functional peak into a Gaussian of half-width σ .

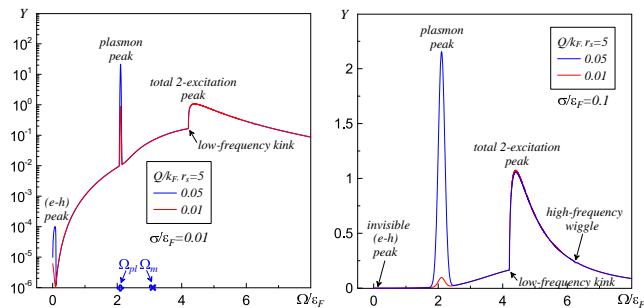


FIG. 18. (color online) Total intensities, including first and second order processes, as functions of Ω for small values of Q at $r_s = 5$. The data are plotted for $Y = D^{(1)} + D^{(2)}/\Gamma^2$ with Γ defined by $(\Omega_{pl}/\Gamma)^2 = 0.1$. The single-plasmon δ -function, Eq. (8), is replaced by a Gaussian with half-width $\sigma = 0.01\varepsilon_F$ (left panel) and 0.1 (right panel). Blue symbols in the left panel mark Ω_{pl} and Ω_m for $r_s = 5$.

The log scale in the figure for $\sigma = 0.01\varepsilon_F$ is taken to demonstrate the entire curves, including the plasmon peak. Since that peak is too narrow, we also present the figure for $\sigma = 0.1\varepsilon_F$ - this width is taken for the reader to easier gauge the total intensity from the area under the curve. From curves for $\sigma/\varepsilon_F = 0.01$ one sees that the $e-h$ contribution is strongly suppressed while the plasmon one, as originating from δ -function, is still comparable to the second-order processes amplitudes even at $Q/k_F = 0.01$ (but peaks are very narrow, of course). In the set of curves for $\sigma/\varepsilon_F = 0.1$ one can not see the $e-h$ contribution, but the plasmon one is still visible even for $Q/k_F = 0.01$ (however, it is strongly suppressed).

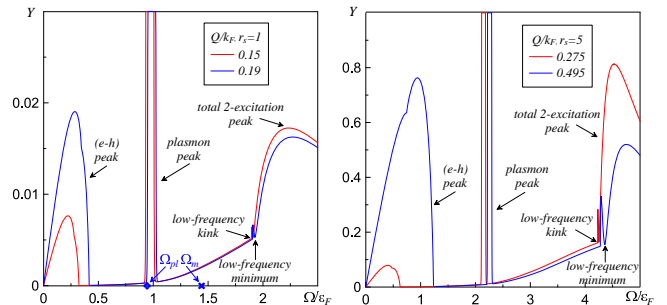


FIG. 19. (color online) Same as in Fig. 18, but for larger values of Q at $r_s = 1$ (left panel) and 5 (right panel). $(\Omega_{pl}/\Gamma)^2 = 0.1$. The Gaussian half-width is $\sigma = 0.01\varepsilon_F$ and plasmon peaks have been cut to fit into the figures. Blue symbols in the left panel mark Ω_{pl} and Ω_m for $r_s = 1$.

In Fig. 19 we plot the total spectrum at $r_s = 1$ and 5 for a few larger values of momentum transfer Q , when intensities of single-excitation processes are not small, but single and multi-excitation processes still do not overlap. In these figures one can also see the low-frequency two-plasmon minima. In both these figures the minima are rather narrow (especially for $r_s = 1$), but well seen.

VII. CONCLUSIONS

We have used the Feynman diagram approach to study the indirect RIXS processes in Coulomb systems in the limit of short core-hole life time. We have discussed the single- and two-excitation processes. For the latter we have provided a comprehensive semi-quantitative picture of their contributions. We have demonstrated the need to account for such excitations at small momentum transfer because the single particle contribution here is suppressed by the size of the matrix element. We have further argued that in the limit under consideration, higher-order processes are suppressed and can be neglected.

We have demonstrated that the multi-excitation processes are important from both the fundamental and practical perspectives by showing how to extract the single-plasmon dispersion from the total two-excitation intensity. This can be done by analyzing the universal spectral features of intensity curves revealed in our work. It is worth mentioning that depending on experimental conditions the sharp plasmon resonance at low momenta may be rather difficult to observe because its intensity vanishes in the $Q \rightarrow 0$ limit (in contrast to the multi-excitation processes). The intensity vanishing at $Q \rightarrow 0$ is also a characteristic feature of the single electron-hole process.

Our analysis is based on the Random Phase Approximation. We believe that this approximation does not qualitatively affect the universal properties of RIXS spectra in metals which originate from thresholds in the particle emission. However, there is no doubt that to obtain quantitatively accurate results for large values of r_s , one has to go beyond RPA to account for the renormalization of the Fermi-liquid parameters and vertex corrections. This constitutes the main direction for the future work.

VIII. ACKNOWLEDGEMENTS

-
- ¹ A. Kotani and S. Shin, *Rev. Mod. Phys.* **73**, 203 (2001).
- ² L. J. Ament, M. van Veenendaal, T. P. Devereaux, J. P. Hill, and J. van den Brink, *Rev. Mod. Phys.* **83**, 705 (2011).
- ³ F. Vernay, B. Moritz, I. Elfimov, J. Geck, D. Hawthorn, T. Devereaux, and G. Sawatzky, *Phys. Rev. B* **77**, 104519 (2008).
- ⁴ C.-C. Chen, B. Moritz, F. Vernay, J. N. Hancock, S. Johnston, C. J. Jia, G. Chabot-Couture, M. Greven, I. Elfimov, G. A. Sawatzky, and T. P. Devereaux, *Phys. Rev. Lett.* **105**, 177401 (2010).
- ⁵ M. Guarise, B. Dalla Piazza, H. Berger, E. Giannini, T. Schmitt, H. Ronnow, G. Sawatzky, J. van den Brink, D. Altenfeld, I. Eremin, and M. Grioni, *Nature Communications* **5** (2014).
- ⁶ M. Dean, *Journal of Magnetism and Magnetic Materials*, **376**, 3 (2015).
- ⁷ A.M. Tsvetlik, R.M. Konik, N.V. Prokof'ev, and I.S. Tupitsyn, *Phys. Rev. Research* **1** (3), 033093 (2019).
- ⁸ R. S. Markiewicz, J. J. Rehr, and A. Bansil, *Phys. Rev. Lett.* **112**, 237401 (2014).
- ⁹ M. Kanasz-Nagy, Y. Shi, I. Klich, and E. A. Demler, *Phys. Rev. B* **94**, 165127 (2016).
- ¹⁰ Y. Shi, A. James, E. Demler, and I. Klich, *Phys. Rev. B* **96**, 155101 (2017).
- ¹¹ M. Hepting, L. Chaix, E. W. Huang, R. Fumagalli, Y. Y. Peng, B. Moritz, K. Kummer, N. B. Brookes, W. C. Lee, M. Hashimoto, T. Sarkar, J.-F. He, C. R. Rotundu, Y. S. Lee, R. L. Greene, L. Braicovich, G. Ghiringhelli, Z. X. Shen, T. P. Devereaux, and W. S. Lee, *Nature* **563**, 374-378 (2018).
- ¹² T. Nomura and J. Igarashi, *J. Phys. Soc. Jpn.* **73**, 1677 (2004); *Phys. Rev. B* **71**, 035110 (2005).
- ¹³ P. M. Platzman and E. D. Isaacs, *Phys. Rev. B* **57**, 11107 (1998).
- ¹⁴ T. P. Devereaux, A. M. Shvaika, K. Wu, K. Wohlfeld, C. J. Jia, Y. Wang, B. Moritz, L. Chaix, W.-S. Lee, Z.-X. Shen, G. Ghiringhelli, and L. Braicovich, *Phys. Rev. X* **6**, 041019 (2016).
- ¹⁵ A. M. Shvaika, O. Vorobyev, J. K. Freericks, T. P. Devereaux, *Phys. Rev. B* **71**, 045120 (2005).
- ¹⁶ J. Lindhard, *Mat. Fys. Medd. K. Dan. Vidensk. Selsk.* **28**, 1 (1954).
- ¹⁷ B. Mihaila, arXiv:1111.5337 (2011).